3D effects on hydrogen transport in ITER-like monoblocks

Rémi Delaporte-Mathurin, Romain Chochoy, Jonathan Mougenot, Yann Charles, Etienne A Hodille, Christian Grisolia

OPEN ACCESS
IOP Publishing | International Atomic Energy Agency
Nuclear Fusion
Nucl. Fusion **64** (2024) 026003 (9pp)
https://doi.org/10.1088/1741-4326/ad1019

3D effects on hydrogen transport in ITER-like monoblocks

Rémi Delaporte-Mathurin[1,2,3,*], Romain Chochoy[2], Jonathan Mougenot[2], Yann Charles[2], Etienne A. Hodille[1] and Christian Grisolia[1]

[1] CEA, IRFM/GCFPM, F-13108 Saint-Paul-lez-Durance, France
[2] Université Sorbonne Paris Nord, Laboratoire des Sciences des Procédés et des Matériaux, LSPM, CNRS, UPR 3407, F-93430 Villetaneuse, France
[3] Plasma Science and Fusion Center, Massachusetts Institute of Technology, Cambridge, MA 02139, United States of America

E-mail: rdelaportemathurin@gmail.com

Received 9 November 2022, revised 31 October 2023
Accepted for publication 27 November 2023
Published 15 December 2023

Abstract

The influence of recombination on the poloidal gaps of ITER-like monoblocks on hydrogen transport simulations is investigated. A 3D FESTIM model is first built and transient simulations up to 1×10^7 s of continuous exposure are run with or without instantaneous recombination on the poloidal gaps. In the case of instantaneous recombination, the poloidal gaps act as a strong sink for hydrogen leading to a decrease in the monoblock inventory. The total desorption flux on the poloidal gap is greater than on the toroidal gap but remains orders of magnitude lower than the retro-desorbed flux at the top surface. For a monoblock thickness of 4 mm, the relative difference in the hydrogen inventory per unit thickness between the two cases is 500%. As the thickness of the monoblock increases, this difference decreases (55% at 14 mm). The monoblock's response to baking is then studied at different baking temperatures. At 600 K, almost all the hydrogen content in the monoblock is removed after 15 days of baking. Assuming a non-instantaneous recombination on the tungsten surfaces would not have a major impact on the monoblock desorption for baking temperatures above 600 K.

Keywords: hydrogen transport, plasma material interactions, modelling

(Some figures may appear in colour only in the online journal)

1. Introduction

Plasma facing materials in fusion reactors such as ITER and DEMO will be submitted to extreme conditions [1]. The tungsten divertor of ITER—made of monoblocks—demonstrated that it met the requirements for high heat flux [2]. Even though some studies proposed alternative designs for DEMO monoblocks [3–5], the ITER-like monoblock concept has been selected in the baseline of DEMO [6].

Bombardment of high energy hydrogen particles (deuterium and tritium) on the tungsten divertors will lead to a build-up of hydrogen inventory, which can induced embrittlement [7] and therefore reduce the component lifetime. Because tritium can be trapped, permeate through materials and contaminate the coolants, it also a radioactive hazard. The control and assessment of this tritium inventory is therefore crucial [8] and it will be optimised to remain as low as reasonably achievable. That is why a maximum inventory of 1 kg of tritium in the vacuum vessel at any time is set as a design constraint [9]. Baking of the plasma-facing-components could reduce the tritium inventory in the divertor

* Author to whom any correspondence should be addressed.

[10]. For the ITER baking phase, the divertor's monoblocks will be kept at a homogeneous temperature up to one month, by heating from the cooling tube.

Hydrogen transport in ITER relevant materials has already been modelled numerically, based on the McNabb and Foster equations [11], with 1D simulations for large sets of radiations conditions [12–16]. 2D simulations for large sets of radiations conditions [17, 18] were also done assuming no effect of the block axial thickness due to the large size defined for ITER design (12 mm). Since the conceptual design for the DEMO monoblocks can still change, the aim for this study is to explore the impact of the block axial thickness on the retention and permeation during plasma operations. Desorption from both the toroidal and poloidal gaps are also studied during the baking phase.

2. Methodology

Figures 1 and 2 shows the ITER-like monoblock geometry used for this study. The toroidal gap between each monoblock is assumed to be 1 mm. To mimic the CuCrZr pipe continuity, a 0.5 mm extrusion of the pipe on each side of the W armour and Cu joint is done on toroidal axe. The poloidal surfaces Γ_{poloidal} include W and Cu materials.

The model is based on previous works on hydrogen transport (including fickian diffusion and transient trapping) coupled with transient heat transfer [22, 23]. The thermophoresis (Soret) and mechanical field effects are not included in this study. The spatio temporal evolution of the mobile and trapped hydrogen concentrations c_{m} (m^{-3}) $c_{\text{t},i}$ (m^{-3}), respectively, are described by the following reaction-diffusion system:

$$\frac{\partial c_{\text{m}}}{\partial t} = \nabla \cdot (D\,(T)\,\nabla c_{\text{m}}) - \sum \frac{\partial c_{\text{t},i}}{dt} \tag{1}$$

$$\frac{\partial c_{\text{t},i}}{\partial t} = k_{\text{i}}\,(T) \cdot c_{\text{m}} \cdot (n_i - c_{\text{t},i}) - p_{\text{i}}\,(T) \cdot c_{\text{t},i} \tag{2}$$

In equation (1) the first term on the right hand side corresponds to the Fick's law, where $D(T) = D_0 \cdot \exp(\frac{-E_D}{k_B \cdot T})$ is the diffusion coefficient of hydrogen in the considered material in m^2s^{-1}, T the temperature in K and $k_B = 8.6 \times 10^{-5}\,\text{eV}\,\text{K}^{-1}$ the Boltzmann constant. In equation (2), the trapping of mobile particles depends on the number of empty trapping sites $n_i - c_{\text{t},i}$, the amount of mobile particles c_{m} and the rate $k_{\text{i}} = k_{0,\text{i}} \cdot \exp(\frac{-E_{k,\text{i}}}{k_B \cdot T})$ in m^3s^{-1}. The second term describes the detrapping process characterised by the rate $p_{\text{i}} = p_{0,\text{i}} \cdot \exp(\frac{-E_{p,\text{i}}}{k_B \cdot T})$ expressed in s^{-1}.

Two intrinsic traps were set in W, one trap in the Cu inter-layer and one trap in the CuCrZr cooling pipe (see table 1). The materials properties used in the simulations are described in table 2. A chemical potential continuity at interfaces is ensured by the continuity of the ratio c_{m}/S where $S = S_0 \exp(-E_S/k_B\,T)$ is the solubility. This interface condition also ensures the conservation of particle flux [22].

The heat equation is solved in stationary form:

$$0 = \nabla \cdot (\lambda \nabla T) \tag{3}$$

where λ is the thermal conductivity expressed in $\text{W}\,\text{m}^{-1}\text{K}^{-1}$ depends on material and temperature (table 2).

A heat flux is imposed on the plasma-facing surface and a convective flux on the cooling surface (see equation (4)):

$$-\lambda \nabla T \cdot \mathbf{n} = \varphi_{\text{heat}} \quad \text{on } \Gamma_{\text{top}} \tag{4a}$$

$$-\lambda \nabla T \cdot \mathbf{n} = -h \cdot (T_{\text{coolant}} - T) \quad \text{on } \Gamma_{\text{coolant}} \tag{4b}$$

where $\mathbf{n}$ is the outward normal vector, $\varphi_{\text{heat}} = 10\,\text{MW}\,\text{m}^{-2}$, $h = 7 \times 10^4\,\text{W}\,\text{m}^{-2}\text{K}^{-1}$ is the convective heat exchange coefficient and $T_{\text{coolant}} = 323\,\text{K}$ is the coolant temperature. A zero flux condition is imposed on the other surfaces.

A non-homogeneous mobile concentration is assumed at the plasma exposed surface to simulate an implanted source of particles (equation (5*a*)) [24, 25]. Depending on the simulation case, a zero concentration or a zero flux is imposed on the poloidal surfaces, respectively when an instantaneous recombination or an non-instantaneous recombination is assumed on the gaps (equation (5*b*)). A recombination flux is assumed on the cooling surface (equation (5*c*)). The other external surfaces will either be insulated (equation (5*d*)) or an instantaneous recombination (equation (5*e*)) will be assumed.

$$c_{\text{m}} = \frac{\varphi_{\text{imp}} R_p}{D} \quad \text{on } \Gamma_{\text{top}} \tag{5a}$$

$$c_{\text{m}} = 0 \quad \text{or} - D \nabla c_{\text{m}} \cdot \mathbf{n} = 0 \text{ on } \Gamma_{\text{poloidal}} \tag{5b}$$

$$-D \nabla c_{\text{m}} \cdot \mathbf{n} = K_{\text{CuCrZr}} \cdot c_{\text{m}}^2 \quad \text{on } \Gamma_{\text{coolant}} \tag{5c}$$

$$-D \nabla c_{\text{m}} \cdot \mathbf{n} = 0 \quad \text{on } \Gamma_{\text{sym}} \tag{5d}$$

$$c_{\text{m}} = 0 \quad \text{on others} \tag{5e}$$

where $\varphi_{\text{imp}} = 1.6 \times 10^{22}\,\text{H}\,\text{m}^{-2}\text{s}^{-1}$ is the implanted particle flux, $R_p = 1 \times 10^{-9}$ m is the particle implantation depth, $D = D_0\,\exp(-E_D/k_B\,T)$ is the diffusion coefficient in m^2s^{-1}, and $K_{\text{CuCrZr}} = 2.9 \times 10^{-14} \exp -1.92/(k_B T)$ is the H recombination coefficient in CuCrZr expressed in m^4s^{-1} [26]. $k_B = 8.617 \times 10^{-5}\,\text{eV}\,\text{K}^{-1}$ is the Boltzmann constant.

The heat flux is mainly caused by incoming particles at the surface and so depends on the incident particle flux and energy, which vary along the divertor. The set of heat flux $\varphi_{\text{heat}} = 10\,\text{MW}\,\text{m}^{-2}$ and particle flux $\varphi_{\text{imp}} = 1.6 \times 10^{22}\,\text{H}\,\text{m}^{-2}\text{s}^{-1}$ is therefore not necessarily representative of all monoblocks in ITER and corresponds to the hottest point (strike point) on the divertor [18]. This particular hot-point was selected for this study as it is hot enough for hydrogen to diffusion in the bulk. Indeed, for fluxes below $1\,\text{MW}^{-2}$, monoblocks remain around coolant temperature (due to the high thermal conductivity of materials). Lower temperatures meaning a smaller diffusivity and higher trapping effects, hydrogen therefore remains closer to the exposed surface [27]. In this case, the aspect ratio of the problem being much higher, edge effects become negligible and the problem is effectively 1D.

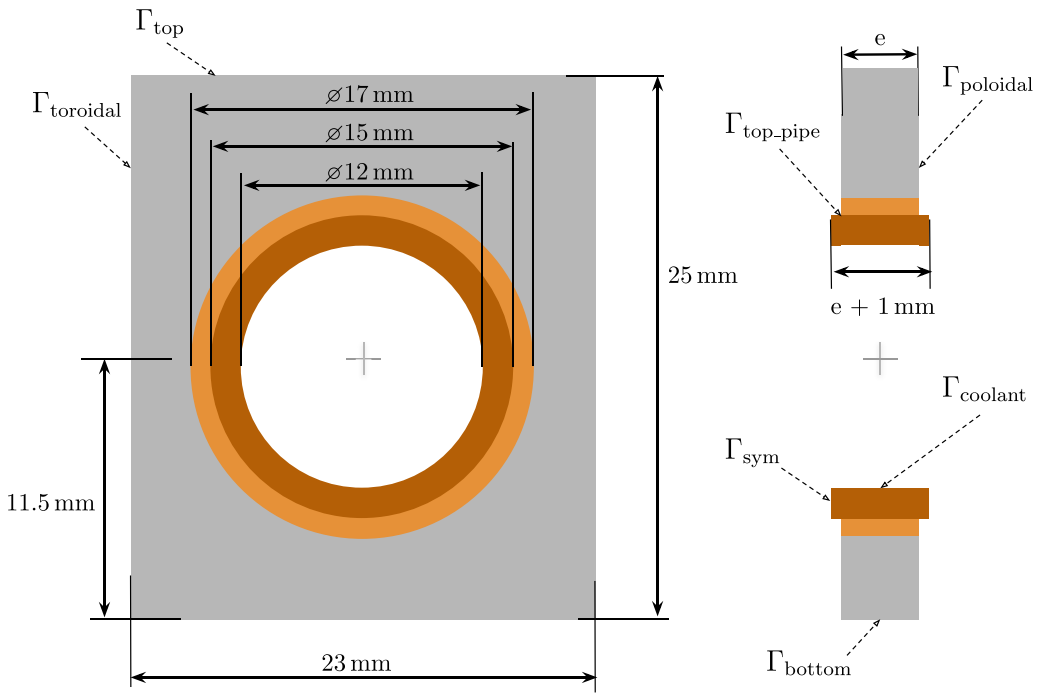

Figure 1. Cross sections of the DEMO monoblock used for this study showing W armour, Cu interlayer, CuCrZr alloy cooling pipe.

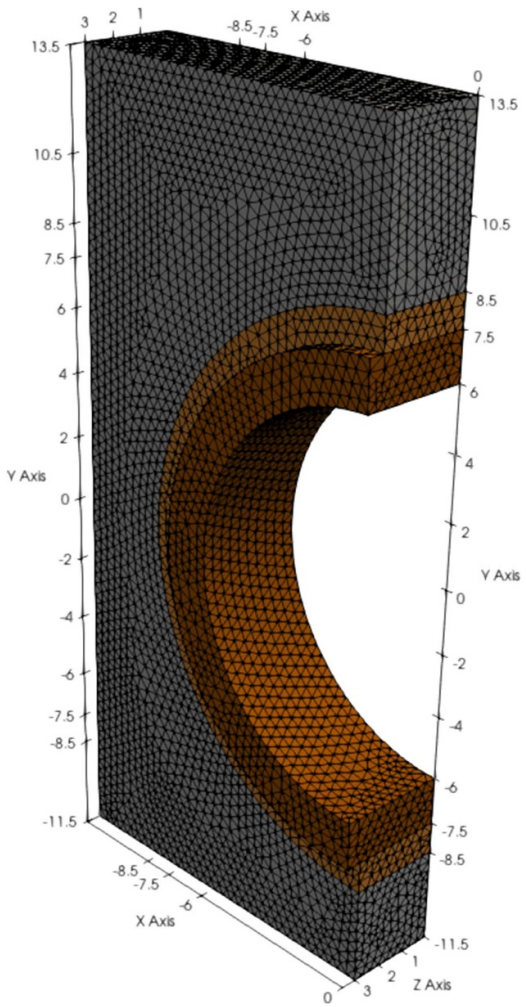

Figure 2. Tetrahedral mesh for $e = 6$ mm made with SALOME corresponding to a quarter of a monoblock (154 130 cells). Units in mm.

Table 1. Traps properties used in the 3D monoblocks simulations.

	Material	$k_0\,(\mathrm{m^3 s^{-1}})$	$E_k\,(\mathrm{eV})$	$p_0\,(\mathrm{s^{-1}})$	$E_p\,(\mathrm{eV})$	n_i (at fr)
Trap 1	W	8.96×10^{-17}	0.39	1×10^{13}	0.87	1.0×10^{-3}
Trap 2	W	8.96×10^{-17}	0.39	1×10^{13}	1.00	4.0×10^{-4}
Trap 3	Cu	6.0×10^{-17}	0.39	8.0×10^{13}	0.50	5.0×10^{-5}
Trap 4	CuCrZr	1.2×10^{-16}	0.42	8.0×10^{13}	0.85	5.0×10^{-5}

Table 2. Materials properties used in the simulations [19–21]. T is the temperature in K.

	Thermal properties		Hydrogen transport properties			
Material	$\rho \cdot C_p(\mathrm{J K^{-1} m^{-3}})$	$\lambda(\mathrm{W m^{-1} K^{-1}})$	$D_0(\mathrm{m^2 s^{-1}})$	$E_D(\mathrm{eV})$	$S_0(\mathrm{m^{-3} Pa^{-0.5}})$	$E_S(\mathrm{eV})$
W	$5.1 \times 10^{-6} \cdot T^3$ $-8.3 \times 10^{-2} \cdot T^2$ $+6.0 \times 10^{2} \cdot T$ $+2.5 \times 10^{6}$	$-7.8 \times 10^{-9} \cdot T^3$ $+5.0 \times 10^{-5} \cdot T^2$ $-1.1 \times 10^{-1} \cdot T$ $+1.8 \times 10^{2}$	4.1×10^{-7}	0.39	1.87×10^{24}	1.04
Cu	$1.7 \times 10^{-4} \cdot T^3$ $+6.1 \times 10^{-2} \cdot T^2$ $+4.7 \times 10^{2} \cdot T$ $+3.5 \times 10^{6}$	$-3.9 \times 10^{-8} \cdot T^3$ $+3.8 \times 10^{-5} \cdot T^2$ $-7.9 \times 10^{-2} \cdot T$ $+4.0 \times 10^{2}$	6.6×10^{-7}	0.39	3.14×10^{24}	0.57
CuCrZr	$-1.8 \times 10^{-4} \cdot T^3$ $+1.5 \times 10^{-1} \cdot T^2$ $+6.2 \times 10^{2} \cdot T$ $+3.5 \times 10^{6}$	$5.3 \times 10^{-7} \cdot T^3$ $-6.5 \times 10^{-4} \cdot T^2$ $+2.6 \times 10^{-1} \cdot T$ $+3.1 \times 10^{2}$	3.9×10^{-7}	0.42	4.28×10^{23}	0.39

Transient simulations up to 1×10^7 s were run, which corresponds to 25 000 plasma discharges of 400 s based on an ITER-like scenario.

The open-source FESTIM code (v0.10.2) [28] was used run the model. All the scripts and datasets to reproduce the results are available at: https://github.com/RemDelaporteMathurin/3d_monoblocks [29]. Since the model has two symmetry planes, only a quarter of the monoblock is modelled as illustrated on figure 2.

3. Results

First, thermal and H transport behaviours during plasma exposure are presented for a standard case ($e = 4$ mm) with and without desorption on the gaps. Next, the influence of the monoblock's thickness (e varying from 4 mm to 14 mm) is shown. The third part is dedicated to the desorption occurring during baking phase. Last, non-instantaneous recombination during baking is discussed.

3.1. Standard case

The temperature field obtained during plasma exposure is shown on figure 3. The top surface temperature of approximately 1200 K. There is no temperature gradient along the poloidal axe because a zero flux condition is imposed on the poloidal surface. The temperature field was therefore similar to a 2D case.

As expected, a higher retention (mobile and trapped hydrogen) was observed in the case without desorption (see figure 4). This is explained by the surface losses (see figure 5).

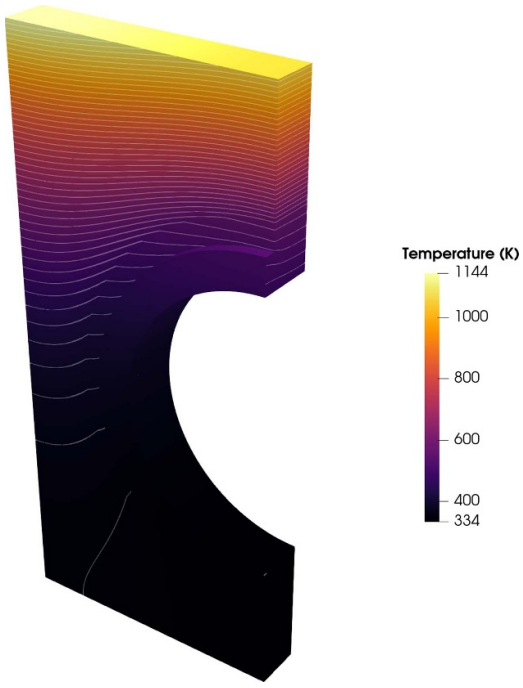

Figure 3. 3D temperature field for $e = 4$ mm.

The total H inventory in the monoblock was also between one and three orders of magnitude lower in the case with desorption (see figure 6). This difference increased with the

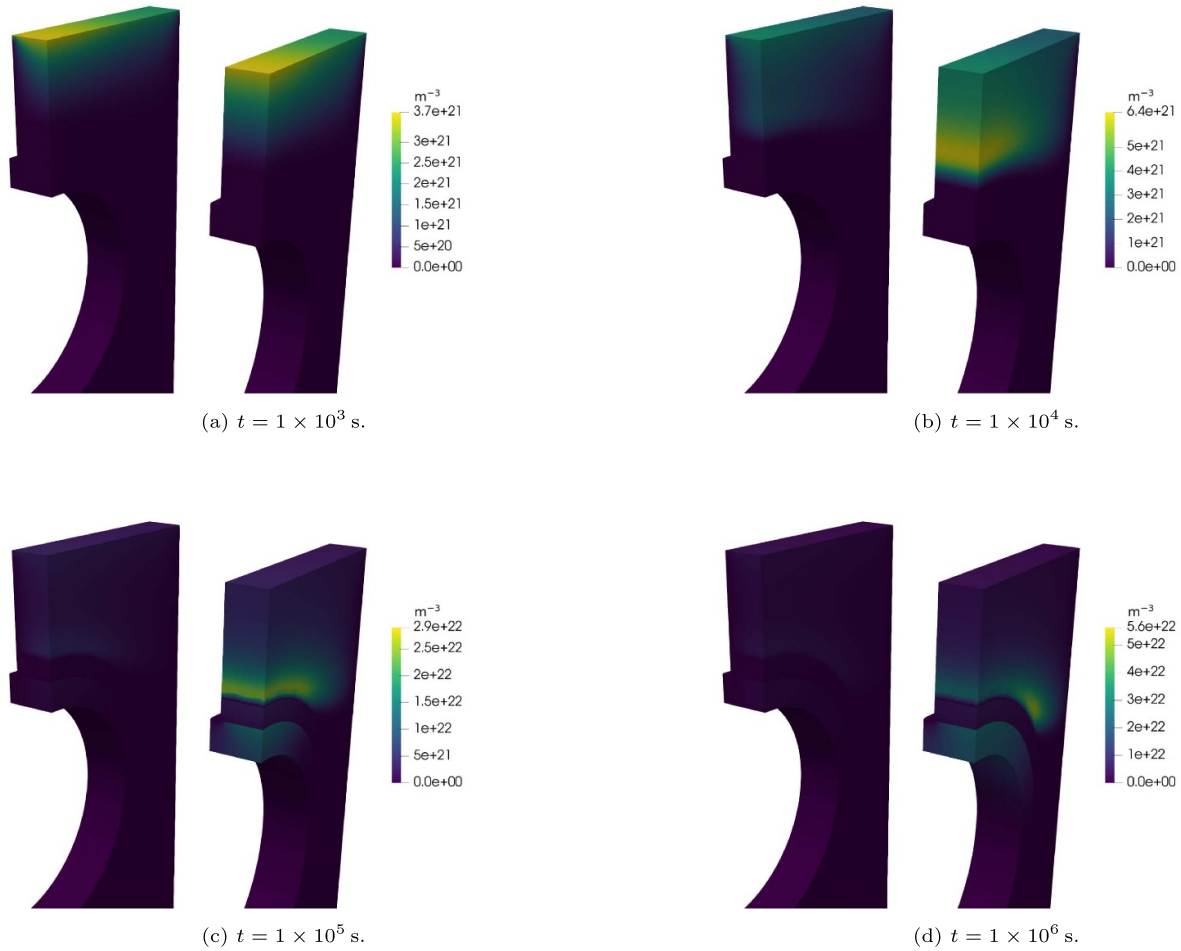

(a) $t = 1 \times 10^3$ s. (b) $t = 1 \times 10^4$ s.

(c) $t = 1 \times 10^5$ s. (d) $t = 1 \times 10^6$ s.

Figure 4. Retention fields of the monoblock with (left) or without (right) recombination on the poloidal gaps (standard case, $e = 4$ mm). Note the colour bars are different.

exposure time. Moreover, the steady state was reached way earlier for the case with desorption whereas the inventory kept increasing after 1×10^6 s for the insulated case. This means that not taking desorption from the gaps into account in 2D simulations is a conservative assumption in terms of H inventory. The 2D simulations performed in previous studies [17, 18, 22, 23, 28] then overestimate the monoblock H inventory (up to a factor 10 after 1×10^6 s) . This conclusion is valid as long as the tritium can desorb from poloidal surfaces i.e. the gaps are in vacuum or pressure free. As studied in [30], some co-deposited materials on the gaps can change the tritium inventory.

These 3D simulations are however essential to estimate the outgassing fluxes from the poloidal gaps. The particle flux at the poloidal gap is six times higher than the flux at the toroidal gap (see figure 7). The permeation flux to the coolant is five to six orders of magnitude lower than the fluxes at the gaps. The particle fluxes at the gaps (poloidal and toroidal) were approximately $1 \times 10^{12}\,\mathrm{H\,s^{-1}}$ whereas the flux towards the cooling channel was below $1 \times 10^{7}\,\mathrm{H\,s^{-1}}$. The values of the outgassing fluxes from both the gaps are orders of magnitude lower than that of the retrodesorbed flux (i.e. the flux of implanted particles that diffuse back to the exposed surface, equal to the implanted flux φ_{imp} assuming a recycling coefficient equal to 1 [25]). This means 3D edge effects will not affect previous results regarding the outgassing to the vessel. They will however impact the value of the contamination flux towards the coolant as assuming an instantaneous recombination on the gaps will lead to way less particles reaching the cooling surface and therefore a lower flux. The flux towards the coolant reaches a maximum close to 1×10^5 s, and next decreases due to the desorption from the top surface of extrusion of the CuCrZr pipe between monoblocks ($\Gamma_{\mathrm{top\_pipe}}$ shown on figure 1).

3.2. Influence of the monoblock thickness

Several simulations were run with monoblock thicknesses varying from 4 mm to 14 mm.

As the thickness increases, the inventory per unit thickness increases for the case with instantaneous recombination on the poloidal gap (see figure 8). It remains constant for the case without recombination and without the CuCrZr extrusion.

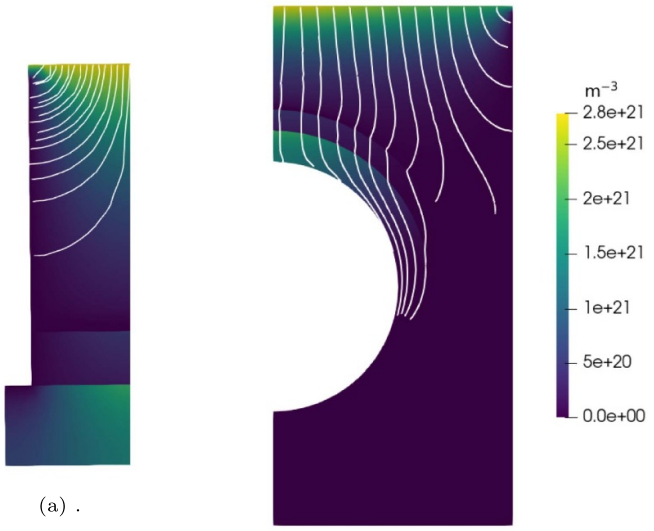

Figure 5. Mobile hydrogen concentration field and stream lines at $t = 1 \times 10^6$ s for the instantaneous recombination case. The streamlines are computed from the gradient of the mobile concentration field.

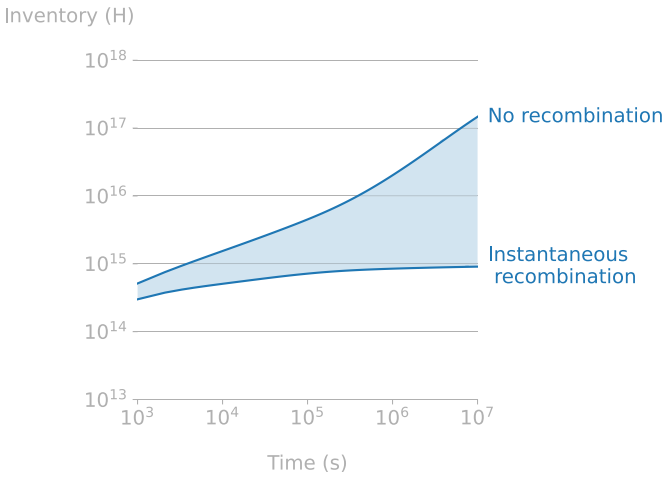

Figure 6. Temporal evolution of the monoblock inventory (standard case).

This case corresponds to a pure 2D case and the inventory is independent of the thickness. The decrease observed at low thicknesses is due to the impact of the CuCrZr pipe between monoblocks $\Gamma_{\text{top\_pipe}}$ as shown on figure 1. The relative difference between the cases with or without recombination on the poloidal gap decreases as the thickness increases. After 1×10^5 s of exposure, for a thickness of 4 mm the relative difference is 500% and drops at 55% for 14 mm. This result was expected as the edge effects become negligible at large thicknesses.

The permeation flux towards the cooling channel per unit thickness globally increases with the monoblock thickness (see figure 9). It is always higher in the case without recombination on the gaps. Similarly to the inventory, the relative

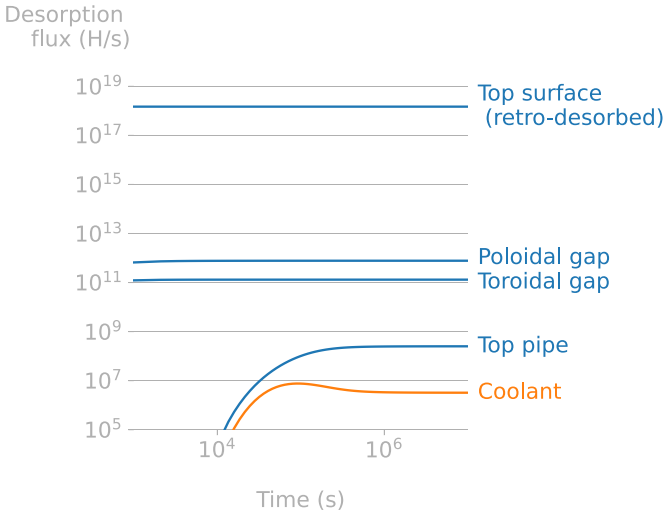

Figure 7. Temporal evolution of outgassing fluxes for the standard case with desorption from the poloidal gaps. Blue lines correspond to the fluxes towards the vacuum vessel, the orange line is the flux towards the coolant.

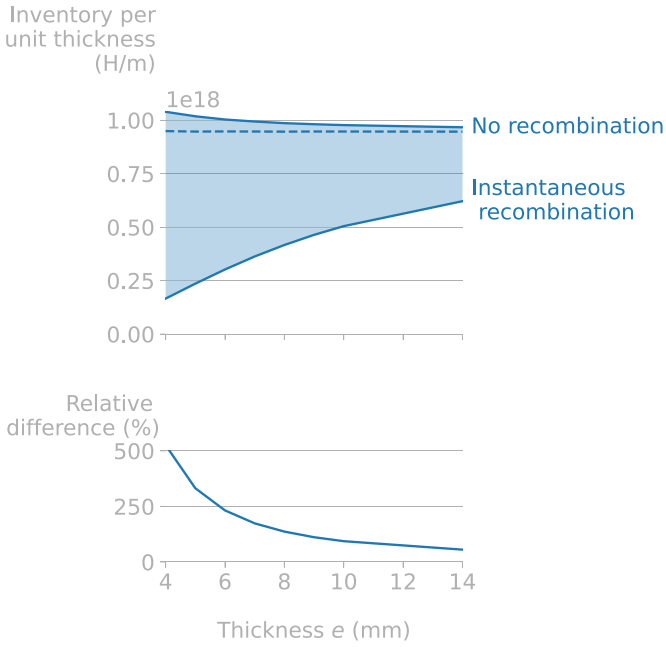

Figure 8. Evolution of the inventory with or without recombination at the poloidal gap for several monoblock thicknesses at $t = 1 \times 10^5$ s. The dashed line represents the case without recombination and without the CuCrZr pipe extrusion.

difference between the cases with or without recombination on the poloidal gap decreases with the thickness.

3.3. Baking

Baking was simulated for 30 days by applying an homogeneous temperature on the monoblock after application of a 10 min temperature ramp between 343 K and the baking set temperature. Instantaneous recombination was assumed

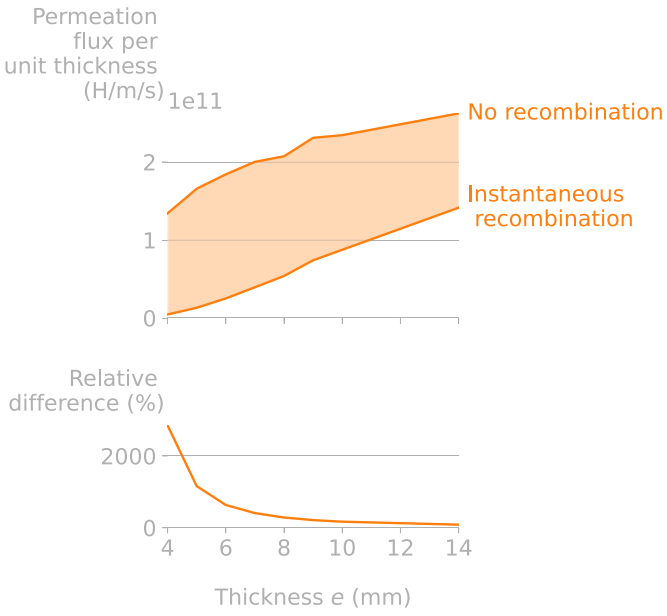

Figure 9. Evolution of the permeation flux to the coolant with or without recombination at the poloidal gap for several monoblock thicknesses at $t = 1 \times 10^5$ s.

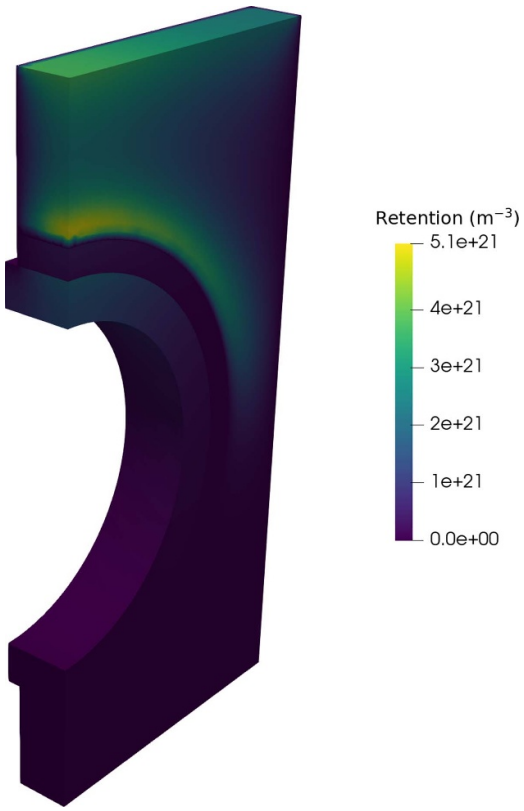

Figure 10. Steady state retention field in the standard case (for $e =$ 4 mm).

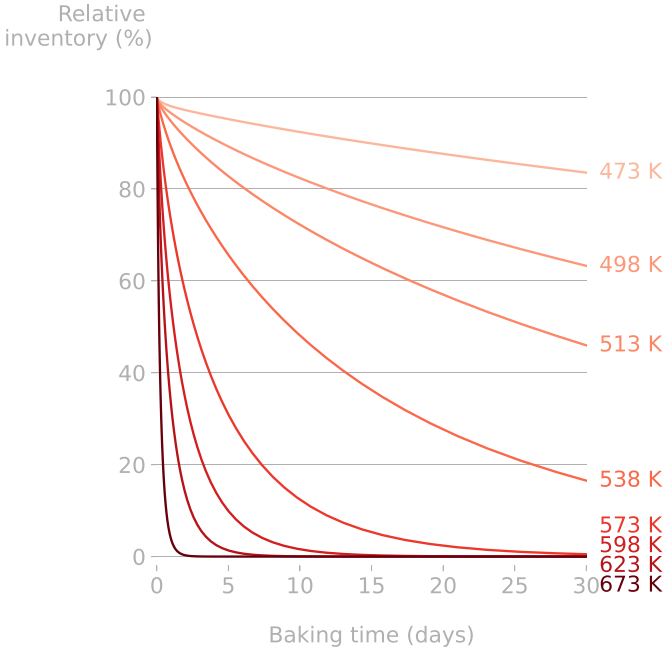

Figure 11. Temporal evolution of the monoblock inventory at several baking temperatures.

on all surfaces (including the cooling surface). Only the initial trapped concentrations were taken from the steady state results of the standard case with desorption on the gaps (see figure 10). The steady state inventory was approximately 1.5×10^{14} H, which corresponds to 2.5×10^{-4} μg. Several temperatures were tested from 500 K to 673 K.

As expected, the monoblock hydrogen inventory decreased for all baking temperatures (see figure 11). The inventory decreased faster at higher baking temperatures. For instance, at 600 K, 5 days of baking are required to decrease the relative inventory to 20%, more than 15 days are required at 550 K. At the highest baking temperature (673 K), the relative inventory is lower than 1% after only 5 days of baking. At the lowest temperature (500 K), after 30 days of baking, more than 60% of the initial inventory still remains in the monoblock.

As for the inventory, the higher the baking temperature, the faster the desorption flux decreases. The desorption from the poloidal and toroidal gaps represents 80% of the total desorption flux (see figure 12). The desorption to the coolant represents ≈10% of the total desorption. Although this value may appear high, it should be noted that it was obtained from a monoblock at steady state. In monoblocks where most of the hydrogen is trapped near the plasma facing surface, the desorption to the coolant is expected to be smaller.

3.4. Influence of non-instantaneous recombination on baking

In the previous simulations, hydrogen was assumed to recombine instantaneously on the surfaces (i.e. the concentration of mobile particle is zero on surfaces). However, a non-instantaneous molecular recombination flux can be applied to surfaces:

$$\varphi_{\text{recombination}} = K_r \, c_{\text{m}}^2 \tag{6}$$

where K_r is the recombination coefficient in expressed in m^4s^{-1} and c_{m} is the concentration of mobile particles.

A recombination flux was set on the tungsten surfaces using Anderl's recombination coefficient [31]:

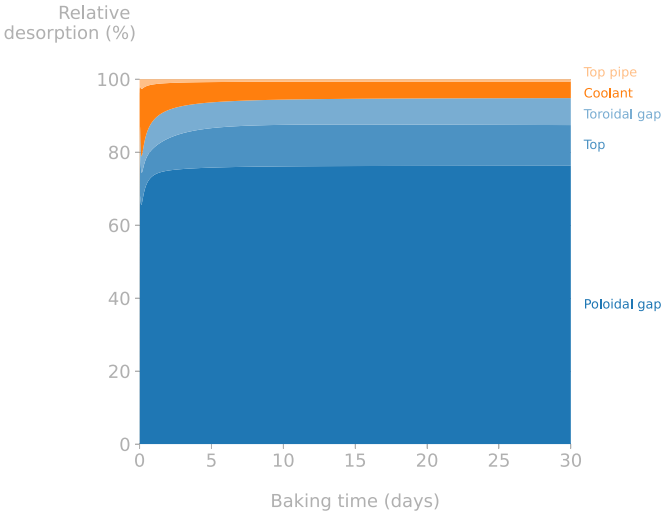

Figure 12. Contribution of the monoblock's surfaces to the total desorption at a baking temperature of 623 K.

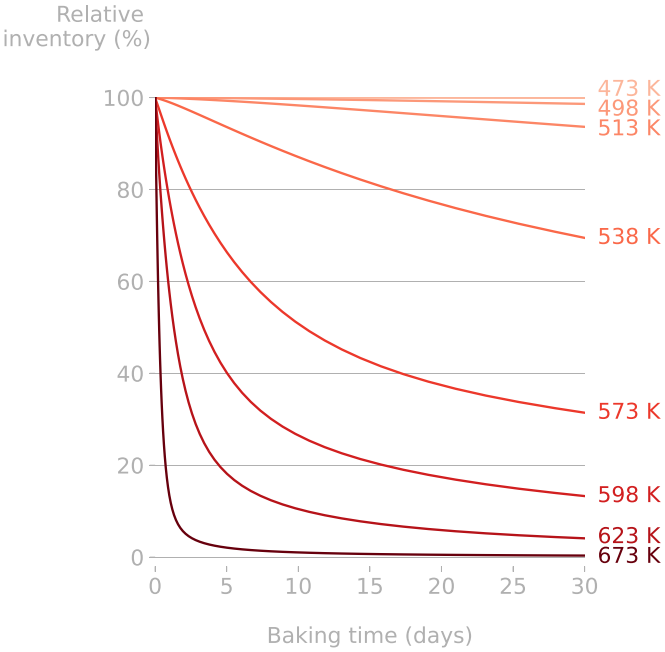

Figure 13. Influence of non-instantaneous recombination on the evolution of the relative inventory for several baking temperatures.

$$K_r = 3.2 \times 10^{-15} \exp(-1.16/k_B T). \quad (7)$$

At high temperature (673 K), there was little difference between instantaneous and non-instantaneous recombination (see figure 13). As expected, at lower temperatures, the non-instantaneous recombination inhibited desorption from the monoblock.

Studies proposed a revised recombination coefficient that would better reproduce experiments [32]. However, this other recombination coefficient has a much higher value. Using this recombination coefficient instead would therefore result in a smaller impact on the desorption.

4. Conclusion

3D edge effects of hydrogen transport in ITER-like monoblocks were studied with the FESTIM code. It was shown that neglecting the desorption from the poloidal gaps leads to an overestimation of the tritium inventory in monoblocks up to a factor four after 10^5 s of plasma exposure for a thickness of 4 mm. This proves that the 2D assumption is conservative in terms of inventory. Moreover, as the thickness of the monoblock increases, the 2D assumption (i.e. neglecting desorption on the poloidal gaps) becomes more valid. For a thickness of 14 mm, the overestimation is reduced to 50%. The 2D assumption is also valid when recombination on the gaps is negligible.

However, these 3D edge effects cannot be neglected when studying baking since the desorption from the poloidal gaps dominates the desorption during baking phases due to the higher surface area. Non-instantaneous recombination on the tungsten surfaces can have an impact on baking at the lowest temperature (below 600 K). At 538 K, the relative inventory after 30 days of baking increases from 20% to 70% with non-instantaneous recombination on the tungsten surfaces. Uncertainties on the recombination coefficients in tungsten and CuCrZr (in contact with water) should therefore be lifted.

Acknowledgments

Plots were produced with Paraview [33], Matplotlib [34], matplotx [35].

The project leading to this publication has received funding from Excellence Initiative of Aix-Marseille University-AMidex, a French 'Investissements d'Avenir' programme as well as from the French National Research Agency (Grant No. ANR-18-CE05-0012). This work has been carried out within the framework of the EUROfusion Consortium, funded by the European Union via the Euratom Research and Training Programme (Grant Agreement No. 101052200 - EUROfusion). Views and opinions expressed are however those of the author(s) only and do not necessarily reflect those of the European Union or the European Commission. Neither the European Union nor the European Commission can be held responsible for them.

ORCID iDs

Rémi Delaporte-Mathurin https://orcid.org/0000-0003-1064-8882
Jonathan Mougenot https://orcid.org/0000-0001-7397-0102
Yann Charles https://orcid.org/0000-0001-8185-7126

Etienne A. Hodille https://orcid.org/0000-0002-0859-390X
Christian Grisolia https://orcid.org/0000-0002-3038-9593

References

[1] Alba R., Iglesias R. and Cerdeira M.A. 2022 Materials to be used in future magnetic confinement fusion reactors: a review *Materials* **15** 6591
[2] Hirai T. *et al* 2016 Use of tungsten material for the ITER divertor *Nucl. Mater. Energy* **9** 616–22
[3] Vizvary Z. *et al* 2020 European DEMO first wall shaping and limiters design and analysis status *Fusion Eng. Des.* **158** 111676
[4] Barrett T.R., Chuilon B., Kovari M., Hernandez D.L., Richiusa M.L., Adame E.R., Tivey R., Vizvary Z., Xue Y. and Maviglia F. 2019 Designs and technologies for plasma-facing wall protection in EU DEMO *Nucl. Fusion* **59** 056019
[5] Domptail F., Barrett T.R., Fursdon M., Lukenskas A. and You J.-H. 2020 The design and optimisation of a monoblock divertor target for DEMO using thermal break interlayer *Fusion Eng. Des.* **154** 111497
[6] You J. *et al* 2021 High-heat-flux technologies for the European demo divertor targets: state-of-the-art and a review of the latest testing campaign *J. Nucl. Mater.* **544** 152670
[7] Temmerman G.D., Hirai T. and Pitts R.A. 2018 The influence of plasma-surface interaction on the performance of tungsten at the ITER divertor vertical targets *Plasma Phys. Control. Fusion* **60** 044018
[8] Abdou M., Riva M., Ying A., Day C., Loarte A., Baylor L.R., Humrickhouse P., Fuerst T.F. and Cho S. 2020 Physics and technology considerations for the deuterium-tritium fuel cycle and conditions for tritium fuel self sufficiency *Nucl. Fusion* **61** 013001
[9] Caruso G. *et al* 2022 DEMO-the main achievements of the pre - concept phase of the safety and environmental work package and the development of the GSSR *Fusion Eng. Des.* **176** 113025
[10] De Temmerman G., Baldwin M.J., Anthoine D., Heinola K., Jan A., Jepu I., Likonen J., Lungu C.P., Porosnicu C. and Pitts R.A. 2017 Efficiency of thermal outgassing for tritium retention measurement and removal in ITER *Nucl. Mater. Energy* **12** 267–72
[11] McNabb A. and Foster P.K. 1963 A new analysis of the diffusion of hydrogen in iron and ferritic steels *Trans. Metall. Soc. AIME* **227** 618–27
[12] Longhurst G.R. 2008 TMAP7 user manual *Technical Report* (Idaho National Laboratory (INL))
[13] Sang C., Bonnin X., Warrier M., Rai A., Schneider R., Sun J. and Wang D. 2012 Modelling of hydrogen isotope inventory in mixed materials including porous deposited layers in fusion devices *Nucl. Fusion* **52** 043003
[14] Schmid K., von Toussaint U. and Schwarz-Selinger T. 2014 Transport of hydrogen in metals with occupancy dependent trap energies *J. Appl. Phys.* **116** 134901
[15] Hodille E.A., Bonnin X., Bisson R., Angot T., Becquart C.S., Layet J.M. and Grisolia C. 2015 Macroscopic rate equation modeling of trapping/detrapping of hydrogen isotopes in tungsten materials *J. Nucl. Mater.* **467** 424–31
[16] Matveev D., Wensing M., Ferry L., Virot F., Barrachin M., Ferro Y. and Linsmeier C. 2018 Reaction-diffusion modeling of hydrogen transport and surface effects in application to single-crystalline Be *Nucl. Instrum. Methods Phys. Res.* B **430** 23–30
[17] Hodille E.A. *et al* 2021 Modelling of hydrogen isotopes trapping, diffusion and permeation in divertor monoblocks under ITER-like conditions *Nucl. Fusion* **61** 126003
[18] Delaporte-Mathurin R. *et al* 2021 Fuel retention in WEST and ITER divertors based on FESTIM monoblock simulations *Nucl. Fusion* **61** 126001
[19] Frauenfelder R. 1969 Solution and diffusion of hydrogen in tungsten *J. Vac. Sci. Technol.* **6** 388–97
[20] Reiter F., Forcey K.S. and Gervasini G. 1996 *A Compilation of Tritium : Material Interaction Parameters in Fusion Reactor Materials* (Publications Office of the European Union)
[21] Serra E., Benamati G. and Ogorodnikova O.V. 1998 Hydrogen isotopes transport parameters in fusion reactor materials *J. Nucl. Mater.* **255** 105–15
[22] Delaporte-Mathurin R., Hodille E., Mougenot J., Charles Y., Temmerman G.D., Leblond F. and Grisolia C. 2021 Influence of interface conditions on hydrogen transport studies *Nucl. Fusion* **61** 036038
[23] Delaporte-Mathurin R., Hodille E., Mougenot J., De Temmerman G., Charles Y. and Grisolia C. 2020 Parametric study of hydrogenic inventory in the ITER divertor based on machine learning *Sci. Rep.* **10** 17798
[24] Hodille E.A., Fernandez N., Piazza Z.A., Ajmalghan M. and Ferro Y. 2018 Hydrogen supersaturated layers in H/D plasma-loaded tungsten: a global model based on thermodynamics, kinetics and density functional theory data *Phys. Rev. Mater.* **2** 093802
[25] Schmid K. 2016 Diffusion-trapping modelling of hydrogen recycling in tungsten under ELM-like heat loads *Phys. Scr.* **T167** 014025
[26] Anderl R.A., Hankins M.R., Longhurst G.R. and Pawelko R.J. 1999 Deuterium transport in Cu, CuCrZr and Cu/Be *J. Nucl. Mater.* **266–269** 761–5
[27] Delaporte-Mathurin R. 2022 Hydrogen transport in tokamaks : estimation of the ITER divertor tritium inventory and influence of helium exposure *These de doctorat* (available at: www.theses.fr/2022PA131054)
[28] Delaporte-Mathurin R., Hodille E.A., Mougenot J., Charles Y. and Grisolia C. 2019 Finite element analysis of hydrogen retention in ITER plasma facing components using FESTIM *Nucl. Mater. Energy* **21** 100709
[29] Delaporte-Mathurin R. and Mougenot J. 2023 RemDelaporteMathurin/3d_monoblocks: revision (available at: https://zenodo.org/record/8091722)
[30] Matveev D., Kirschner A., Schmid K., Litnovsky A., Borodin D., Komm M., Van Oost G. and Samm U. 2014 Estimation of the contribution of gaps to tritium retention in the divertor of ITER *Phys. Scr.* **T159** 014063
[31] Anderl R.A., Holland D.F., Longhurst G.R., Pawelko R.J., Trybus C.L. and Sellers C.H. 1992 Deuterium transport and trapping in polycrystalline tungsten *Fusion Technol.* **21** 745–52
[32] Ogorodnikova O.V. 2019 Recombination coefficient of hydrogen on tungsten surface *J. Nucl. Mater.* **522** 74–79
[33] Ahrens J.P., Geveci B. and Law C. 2005 36 - ParaView: an end-user tool for large-data visualization *Visualization Handbook* eds C D Hansen and C R Johnson (Butterworth-Heinemann) pp 717–31
[34] Hunter J.D. 2007 Matplotlib: a 2D graphics environment *Comput. Sci. Eng.* **9** 90–95
[35] Schlömer N. 2022 Matplotx: extensions for Matplotlib, (available at: https://zenodo.org/record/7015080)